Geometric and kinematic analysis of normal faults bordering continental shelves: A 3D seismic case study from the northwest South China Sea

Shouxiang Hu[a, b, c, d], Tiago M. Alves[e], Kamaldeen O. Omosanya[f], Wei Li[a, b, c, d]*

[a] CAS Key Laboratory of Ocean and Marginal Sea Geology, South China Sea Institute of Oceanology, Chinese Academy of Sciences, Guangzhou 510301, P. R. China
[b] Southern Marine Science and Engineering Guangdong Laboratory, Guangzhou, 511458, China
[c] Innovation Academy of South China Sea Ecology and Environmental Engineering, Chinese Academy of Sciences, Guangzhou 510301, P. R. China
[d] University of Chinese Academy of Sciences, Beijing 100049, P. R. China
[e] 3D Seismic Lab. School of Earth and Ocean Sciences, Cardiff University, Main Building, Park Place, Cardiff, CF10 3AT, United Kingdom
[f] Oasisgeokonsult, 7052 Trondheim
*Corresponding author: Dr. Wei Li (wli@scsio.ac.cn)

Abstract

Normal faults are ubiquitous on many continental shelves, but have only been considered to play a subordinate role to basin-controlling faults in previous basin studies such as Qiongdongnan Basin. Their detailed geometries and kinematic histories are still poorly known. In this study, high-quality three dimensional (3D) seismic data are used to investigate families of normal faults bordering the continental shelf of the northwest South China Sea. Sixty-six (66) normal faults are interpreted and found to mostly tip out in Upper Miocene strata. Three large-scale faults offsetting the base of Pliocene (Horizon T30) and three faults terminating beneath this horizon were selected and studied in detail. We distinguished growth and blind faults according to upper tip folding geometries and fault displacement distributions via throw-depth (T-z) plots. The dips of the upper parts of faults are almost twice that of the lower parts. A new three-stage model for fault reactivation in Qiongdongnan Basin is therefore proposed based on our results. In the northwest South China Sea, the propagation of normal faults on the continental shelf can be attributed to: (1) the rotation of the South China block and a reversal in the movement of the Ailao Shan-Red River Fault Zone from left- to right-lateral slip, and (2) large-scale slope instability in the Qiongdongnan Basin at ~5.5 Ma. The results presented here provide a better understanding of the structural framework and evolution of the continental shelf of the northwest South China Sea from 5.5 Ma to the present day. Importantly, our results also prove that reversals in the movement of margin-scale structures as the Ailao Shan-Red River Fault Zone can control the evolution of normal faults on continental shelves in the Qiongdongnan Basin.

Keywords:

South China Sea; Continental shelf; Qiongdongnan Basin; Ailao Shan-Red River Fault Zone; Fault evolution; Throw-depth plots.

1 Introduction

Normal faults have been studied for more than a century (Willis and Reid, 1907), and are still the focus of intensive research when exploring for new resources, or when completing geohazard assessments (Omosanya et al., 2018; Wu and Hu, 2019; Childs et al., 2020). Normal faults on continental shelves have been largely

ignored in the literature addressing large-scale basin-controlling faults (Sun et al., 2014; Lei and Ren, 2016). Yet, it has been suggested that normal faults can modulate the morphology and geometry of continental shelves (Gomes et al., 2014). They can promote variations in seafloor gradient while, at the same time, controlling sediment accumulation in deep-water sedimentary basins (Soares et al, 2012; 2014; Maier et al., 2017). The activity of normal faults on continental shelves can also trigger submarine slope instability and associated tsunamis (e.g., Gamberi et al., 2011; Rovere et al., 2014). Moreover, detailed investigations of normal faults on continental shelves are key to identify the sources of offshore earthquakes, helping the completion of regional seismic-risk maps (Perea et al., 2018).

In the fields of marine geology and geophysics, the geometries and evolution of normal faults have been extensively studied in the last three decades (Baudon and Cartwright, 2008a; Alves et al., 2009; Tao and Alves, 2016; Perea et al., 2018). Methods for kinematic analyses of normal faults such as throw-depth (T-z) plots, displacement–length plots (D-x) and expansion indices (Wadsworth, 1953; Thorsen, 1963; Dawers et al., 1993), together with the interpretation of high-quality three-dimensional (3-D) seismic datasets, have expanded our understanding of the growth and kinematics of normal faults along the many continental margins (e.g. Baudon and Cartwright, 2008a; Alves et al., 2009; Tao and Alves, 2016; 2019). In parallel, different modes of fault propagation (e.g. modes of upward and dip-linkage reactivation) have been documented in the literature using seismic data, outcrop, and analogue and numerical modeling (Walsh and Watterson, 1988; Cartwright et al., 1995; Baudon and Cartwright, 2008a; Alves et al., 2009). Hence, a comprehensive investigation of normal faults' kinematic histories is key for understanding the evolution of continental margins such as the South China Sea margin.

In recent years, an increasing number of studies have focused on the evolution of basin-controlling faults on the northern South China Sea margin (Fig. 1). For example, Lei et al. (2019) investigated the close relationship between structures and sedimentation within the Liwan Sag and proposed that the activity of detachment faults led to widespread extension in this area. Huang et al. (2018) investigated reactivation of the lower syn-rift fault system in the Pearl River Mouth Basin and presented a four-stage evolution model of the oblique-slip fault zone. In parallel, Zhao et al. (2018a) conducted a study of normal faults in the Baiyun Sag, revealing important relationships between the generation of faults and the regional evolution of the northern South China Sea margin. Despite these new interpretations, few studies have thus far focused on the geometry and evolution of normal faults on the continental shelves bordering the South China Sea. Based on a comprehensive interpretation of high-quality 3D seismic data in the northwest South China Sea (Fig. 1), the main aim of this study is to investigate the propagation histories of 66 normal faults detail, understanding their role in the evolution of the northwestern South China Sea margin (Fig. 1a). The specific aims of this work are to:

(a) determine the general characteristics (strikes, dip, lengths) and distribution of normal faults bordering the continental shelf;

(b) investigate their growth histories since the Late Miocene by using throw-depth plots;

(c) analyse the main factors controlling fault evolution in the northwest South China Sea, and;

(d) discuss their significance in the context of the whole tectono-stratigraphic evolution of the South China Sea.

2 Geological setting

The South China Sea is one of the largest marginal seas in the Western Pacific Ocean, and its evolution is the result of complex tectonic movements at the edges of the Eurasian, the Pacific and the Indo-Australian plates (Fig.1; e.g.

Clift and Sun, 2006). Sedimentary basins along the northern South China Sea margin were first formed by lithospheric stretching during the Paleocene and Oligocene, prior to widespread thermal subsidence (Ru and Pigott, 1986; Xie et al., 2006). At a local scale the focus of this study, the Qiongdongnan Basin, is one of the Cenozoic sedimentary basins developed on the northwestern South China Sea margin (Li et al., 2006; Zhao et al., 2015; Lei and Ren, 2016).

In the context of its regional tectonic framework, the evolution of Qiongdongnan Basin is influenced by the movement of the South China and Indochina tectonic plates (Fig. 1). The South China plate was formed in the Proterozoic with Indochina, similarly to South China, thought to have also been derived from Gondwana in the Early Paleozoic (Hinsbergen et al., 2011; Li et al., 2017). Relative rotation, collision, and movement between the South China and Indochina plates has been recorded since then (Replumaz and Tapponnier, 2003; Van Hinsbergen et al., 2011; Faure et al., 2014). Importantly, the southwestern part of the South China plate became separated by a left-lateral strike slip fault during the Late Cenozoic (e,g., Tong et al., 2015).

The tectono-stratigraphic evolution of the Qiongdongnan Basin includes two main stages: (a) a syn-rift stage spanning from the Paleocene to Oligocene that is marked by extensional tectonics and the development of tectonic faults (Wang et al., 2013; Sun et al., 2014), and (b) a Miocene-Quaternary post-rift stage was characterised by moderate faulting and widespread thermal subsidence (Fig 2; Chen et al., 1993; Zhou et al., 1995; Li et al., 2006; Xie et al., 2006; Zhu et al., 2007b; Wu et al., 2009; Gong et al., 2011).

During the first stage, the Qiongdongnan Basin had deposited the Paleocene to Oligocene alluvial and lacustrine sediments and the Early to Middle Miocene nearshore and neritic sediments (Xie et al., 2006; He et al., 2013). Continental slope systems began to develop during the second stage, which start from the Late Miocene to the present day (Xie et al., 2006; He et al., 2013). Submarine canyons and channels were widely developed during the second stage in response to a more prominent slope-basin physiography (Zhu, 2007; Gong et al., 2011). The asymmetrical shelf break of the northwestern South China Sea margin gradually developed from the Late Miocene to the Pliocene (Xie et al., 2008a; Zhao et al., 2019).

Three distinct groups of syn-rift faults have been previously documented in the Qiongdongnan Basin: NE–SW, E–W and NW–SE striking faults (Fig. 1b; Zhang et al., 2013; Lei and Ren, 2016). The NE-SW striking faults developed throughout the Qiongdongnan Basin whereas NW-SE striking faults occurred in the northwestern to the western part. The E-W striking faults are located in the eastern part of the basin (Xie et al., 2006; Lei et al., 2020).

The Ailao Shan-Red River Fault Zone (comprising an NW-striking zone of strike-slip movement) forms the boundary between the South China and Indochina plates, and also marks the western boundary of the Qiongdongnan Basin (Fig 1; Clift and Sun, 2006; Zhu et al., 2009; Lei et al., 2011; Lei et al., 2015). Predominantly left-lateral movement of the Ailao Shan-Red River Fault Zone is documented at ~30 Ma based on kinematic indicators and thermochronological evidence available from its onshore part (e.g. Leloup et al., 2001; Gilley et al., 2003). Left-lateral displacement of the Ailao Shan-Red River Fault Zone was estimated between 500 to 1400 km (Searle et al., 2010; Leloup et al., 2001). In the period spanning 16 Ma and 5.5 Ma b.p., the Ailao Shan-Red River Fault Zone experienced a shift from a sinistral to a dextral movement (e.g. Replumaz et al., 2001; Zhu et al., 2009), changing to a predominant dextral movement after 5.5 Ma (Sun et al., 2003; Zhu et al., 2009).

3 Data and methods

3.1 3D seismic data

This study is based on ~550 km^2 of high-quality 3D seismic reflection data acquired by the China National Offshore Oil Corporation (CNOOC). The acquisition geometry for the seismic produced seismic traces spaced by 12.5 m, with inlines that are oriented ENE and crosslines in NNW direction. The acquisition vessel used a 3000 m-long streamer with 240 channels.

The seismic data is zero-phased at the sea floor and troughs (red reflections) represent a relative decrease in acoustic impedance and peaks (black reflections) correspond to an increase in acoustic impedance. The main frequency bandwidth of the seismic data is 30-45 Hz and its dominant frequency is 35 Hz. With a velocity of 1500 m/s, the seismic data has a vertical resolution approaching 10 m near the sea floor. The seismic volume images the continental shelf of the northwest South China Sea at a water depth of approximately 250 m (Fig.1) in Qiongdongnan Basin.

3.2 Fault analysis

Throw-depth (T-z) plots record the absolute throws of faults and highlight specific phases of fault nucleation, growth, and propagation (Mansfield and Cartwright, 1996; Cartwright et al., 1998). Fault throw (T) is equal to the difference between the vertical distance of correlative strata on the footwall and immediate hanging wall of a fault (Omosanya et al., 2015) and were estimated on faults using seismic profiles perpendicular to the fault strike (Mansfield and Cartwright, 1996). Hence, T-z plots depict differences in throw against depth of correlative strata along and across normal faults (Fig. 3). Variations in the gradient of T-z plots indicate growth and non-growth periods with (i) null-slopes (K=0) representing periods of no-growth, (ii) positive slopes (K>0) indicating growth periods (Cartwright et al., 1998), and (iii) negative slopes (K<0) reflecting the reversal of movement in faults, or fault overlap and linkage during the propagation of distinct segments (Fig. 3; Mansfield and Cartwright, 1996). T-z plots of blind faults show classical patterns approaching M- or C-type profiles (Fig. 3b; Baudon and Cartwright, 2008c).

Uncertainties in the use of T-z plots relate to burial-related compaction in sediment (Taylor et al., 2008; Giba et al., 2012) as compaction may cause deviations in the thickness of hanging-wall and footwall strata. However, compaction can be ignored as the compaction loss is minor for growth faults, reaching a maximum compaction of <20% at a sub-surface depths of ~ 0.5 to 4 km (Taylor et al., 2008; Giba et al., 2012). To describe the central value and effectively reduce the impact of deviation, we also use the average value of what?, ~~which is the sum of the values divided by the number of values,~~ to improve accuracy.

In this paper, we have primarily mapped fault-throw variations with Fault 1 being selected as a key example (Fig. 4). T-z plots are displayed in two-way travel-time (TWTT) as velocity (V_p) information was not available around Fault 1. To verify whether this simplification could cause significant distortions to the patterns of vertical throw variation, we used velocity data from nearby wells to depth-convert our measurements (Zhao et al., 2015). The depth converted T-z plot in Fig. 4 shows similar T-z distributions in both time (Fig. 4a) and depth (Fig. 4b) to its two-way time counterpart, and the parameter K also shows similar trends. The lower parts of faults below Horizon T30 are generally characterised by a negative gradient (-0.07 and -0.06), with their central and upper portions exhibiting positive throw gradients (Fig. 4a and 4b). Significantly, Figure 4 shows that tectonic subsidence, changes in local depositional rates, including compaction and erosional processes, did not affect the shape of the T-z plots (Zhao et al., 2018b).

4 Results

4.1 Regional seismic stratigraphy

Three main horizons T40 (10.5 Ma), T30 (5.5 Ma), T20 (1.9 Ma) and the sea floor were mapped and correlated to regional stratigraphic units based on the stratigraphic framework of Xie et al. (2006, 2008b) (Fig. 5). Horizon T40 is a high- to moderate-amplitude seismic reflection corresponding to the base of the Huangliu Formation (Fig. 5a). Horizon T30 is a seismic reflection of high-amplitude with good lateral continuity and represents the top surface of the buried submarine canyons (Fig. 5b). Chronologically, T30 corresponds to the base of the Yinggehai Formation. The Quaternary/Pliocene boundary or base of the Ledoing Formation was mapped as Horizon T20, a high-amplitude seismic reflection (Fig. 5b). All these three horizons can be traced across the study area and bound three main stratigraphic units (Units 1, 2 and 3).

4.1.1 Unit 1

Unit 1 is bounded by T40 (10.5 Ma) and T30 (5.5 Ma), comprising Upper Miocene strata. Unit 1 shows discontinuous to chaotic internal seismic reflections towards the southeast of the seismic volume, with subsequent reflections becoming continuous to the northwest (Fig. 5a). The thickness of Unit 1 varies between 550 ms TWTT in the northwest to 950 ms TWTT in the southeast (Fig. 5b). In addition, several faults terminate below Horizon T40, while other large-scale faults propagate above Unit 1 (Fig. 5a). Horizon T40 marks the acceleration of thermal subsidence in the Qiongdongnan Basin (e.g. Han et al., 2016), when submarine canyons were widely developed in Unit 1 (Fig. 5b). The width of these submarine canyons ranges between 500 m to 5000 m and they have the length of 10 km to over 30 km (Fig. 5b).

4.1.2 Unit 2

Unit 2 is Pliocene in age and is bounded at its base by horizon T30 and at its top by horizon T20 (1.9 Ma; Fig. 5). Internal seismic reflections in Unit 2 are similar to those in Unit 1, i.e. they are continuous in the northwest and chaotic in the southeast (Fig. 5a). The thickness of Unit 2 increases from 450 ms TWTT to 650 ms TWTT towards the southeast, but it does not change significantly in a NE–SW direction (Fig. 5b). Horizon T30 (~5.5 Ma) is an important seismic-stratigraphic marker in the study area due to its continuity. It also correlates with a marked sea-level lowstand (red dot in Fig. 2) which resulted in widespread incision of submarine canyons and channels in the South China Sea (Wei et al., 2001; Sun et al., 2010; Wang et al., 2013). Some faults terminate in Unit 2, whereas large-scale faults propagate above Horizon T20 (Fig. 5a).

4.1.3 Unit 3

Unit 3 comprises Quaternary sediments bounded by Horizon T20 (1.9 Ma) and the sea floor. It is mainly characterised by its parallel to sub-parallel, continuous internal reflections (Fig. 5a). Unit 3 shows a constant thickness of ~390 ms TWTT and it is intersected by few faults (Fig. 5a).

4.2 Distribution, geometry and timing of normal faults

In total, 66 normal faults were mapped in the 3D seismic survey (Fig. 6). The strikes of 88% of these faults range from N90 to N139, and only 17 faults strike between N110 and N130 (Fig. 6). In plan view, most of the faults occur in the north, are less than 5 km long, and are essentially parallel to each other. This is chiefly the case for faults whose length is less than 5 km (Fig. 6b). Conversely, normal faults in the south of the study area are more than 5 km long. The longest normal fault is approximately 20 km long and located in the south-central part of the study area (Fig. 6). Most of the interpreted faults dip in a SE direction, with a few antithetic faults forming small graben-like structures (e.g., Figs. 5 and 7). Furthermore, the majority of the interpreted faults terminate below Horizon T30 and have dip angles of 19°-25° in seismic profiles. The faults

that terminate in Unit 1 (Miocene) show dip changes with depth, particularly near Horizon T30. Faults show an average dip of around 20° below Horizon T30, while they can reach dips of 45° above this same horizon (e.g. Fig. 4). Importantly, there are obvious differences in dip when comparing the upper and lower parts of these normal faults (e.g. Fig. 4).

In terms of depth distribution, most normal faults show their upper tips below Horizon T20 and approximately 30% of all faults terminate below Horizon T40 in the northern part of the study area. In turn, about 45% of the faults are truncated between T30 and T40 (Unit 1). A distinct group of normal faults (25% of the total faults mapped) propagated through T30 to terminate in Pliocene strata (Unit 2). As for the large-scale normal faults, only 5% offset Quaternary strata (Unit 3) (Fig. 7a). Towards the southeast, the number of faults decreases sharply, with most faults being truncated between Horizons T30 and T40 (Unit 1), and the remainder occurring under Horizon T40 (Fig. 7b). Most of the interpreted faults offset Middle Miocene to Pliocene strata (Unit 2) in the central part of the study area, and only few faults terminate within Unit 3 (Fig. 7b). There is only one fault in the southern part of the study area that terminates in Quaternary strata (Unit 1; Figs. 6 and 8a).

4.3 Kinematic and growth history of normal faults

Subtle changes in vertical throw can be observed because of the good vertical resolution (c. 10 m) of the seismic data. In order to record vertical variations in throw distributions, three large-scale faults (Faults 1, 2, and 3), and three small-scale faults terminating below T30 were selected for a detailed T-z analysis (Fig. 6). Fault 1 is located at the edge of the continental shelf and is the lengthiest in the southern part of the study area (10 km maximum long). Fault 2 is located in the middle section of three large-scale faults (10 km maximum long), where small-scale faults are also observed. Fault 3 (11 km maximum long) occurs in the northern part of the study area. The three small faults are located in the northern and middle parts of the study area (Fig. 6).

4.3.1 Fault 1

Fault 1 can be divided into two main segments based on the observed changes in strike and plan-view curvature (Fig. 6). The two segments of Fault 1 roughly strike to the E. The average dips of the upper part of Fault 1 range from 40° to 45°. In contrast, the dip of the lower part of Fault 1 approaches 23° below Horizon T30 (Fig. 4a). The throw distribution for the whole fault plane (Fig. 8a) is characterised by a hybrid pattern similar to the M-type of Muraoka and Kamata (1983). The maximum throw of Fault 1 ranges from 65.2 to 90.7 ms TWTT close to Horizon T30 in different seismic profiles (Fig. 8a). The upper tips of Fault 1 terminate roughly at the same stratigraphic interval (c. 310 -329 ms) within Quaternary strata. In Unit 1, the lower part of Fault 1 (below T30) is generally characterised by negative gradients between -0.03 and -0.07 (Fig. 8a). The central portion of this fault exhibits throw gradients ranging from 0.03 to 0.09 (average 0.06). In contrast, T-z data for Fault 1 show near-constant positive gradients in Unit 2 with decreasing throws with depth (Fig. 8a). Similarly, the throw values for Fault 1 continue to decline with small variations in Unit 3, where it is charaterised by steep throw gradients in which the parameter K reaches 0.09 (Fig. 8a).

4.3.2 Fault 2

Fault 2 strikes to the SE and has a maximum length of 10 km (Fig. 6b). Changes in dip above and below Horizon T30 are common in Fault 2. The upper tips of Fault 2 terminate at a depth around 440 ms TWTT, within the Quaternary strata (Fig. 9a). The vertical throw distribution for Fault 2 shows marked changes in gradient. Steeper gradients occur in the upper tip region (average gradient up to 0.09 in the upper part and

0.03 in the lower part). Maximum throws in Fault 2 are 47.24 ms (northwestern part) and 69.42 ms (southeastern part), respectively (Fig. 8b). The T-z plot of Fault 2 shows a decrease in throw values in its tip region. The average throw values of the three parts composing the fault are 58.33, 29.85, and 14.26 ms, respectively, decreasing from the lower to the upper tips of the fault.

4.3.3 Fault 3

Fault 3 is located in the northern part of the study area, on the continental shelf (Fig. 6) and strikes to the SSE with a maximum length of 11 km (Fig. 6). The T-z plots for Fault 3 are half-elliptical in shape (Fig. 8c). The largest throw gradient occurs in the middle of the T-z plots. The upper tips of Fault 3 terminate at around 450 ms TWTT in Quaternary strata. T-z data for Fault 3 show throws of up of 40 ms TWTT in Unit 1 with an average gradient close to zero (K ~ 0.001; Fig. 8 c). The average throw (28.8 ms) in this Unit is the largest for this fault. Fault 3 shows a positive gradient from Unit 2 to Unit 3 (Fig. 8c).

4.3.4 Faults terminating below Horizon T30

Most faults (~74%) in the study area terminate below Horizon T30. These faults are relatively small, strike to the WNW, and show average dips between 17° to 31° (Fig. 9d). Their upper tips terminate at different stratigraphic intervals within mid and upper Miocene strata (c. 1420-2057 ms). However, we note that adjacent faults do not terminate at the same depth in the study area (Figs. 5a and 7a). Vertical throw plots for faults terminating below Horizon T30 tend to be asymmetrical C-types with some degrees of variation (Fig. 8d; Muraoka and Kamata, 1983). The throw maxima of these faults are concentrated in Middle Miocene strata, where throws of 51 to 59 ms are gathered (Fig. 8d). The interval below Horizon T30 accommodated the majority of fault growth and is characterised by its steep gradient where K reaches 0.26. All the T-z plots show fault throws increasing moderately to then decrease sharply in mid and upper Miocene strata. In addition, the T-z plots reveal some near-zero gradient segments below Horizon T40 (see yellow lines in Fig. 8d).

5 Discussion

5.1 Nucleation, propagation and kinematic history of normal faults

The displacement patterns of small growth faults with slow, regular episodes of displacement can be remarkably similar to blind faults (Petersen et al., 1992; Childs et al., 1993; Nicol et al., 1996). The growth package is one of the unequivocal characteristics of the growth fault (e.g. Thorsen, 1963; Baudon and Cartwright, 2008c). However, near many small growth faults is much harder to recognise growth packages (Childs et al., 2003). In our study area, it may be impossible to determine whether the faults without growth packages are growth faults or blind faults. However, the high-quality 3D seismic data and detailed throw-depth analysis in this work allowed us to determine whether we are in the presence of growth or blind faults. According to the original definition of blind faults in Watterson (1986), and the criteria for the recognition of blind faults proposed by Baudon and Cartwright (2008c), two lines of evidence are proposed here to classify the normal faults in our study area.

The first line of evidence is related to the upper tip lines imaged in the T-z plots of the interpreted faults (Fig. 8). According to Baudon and Cartwright (2008c), the upper tip line of blind faults commonly shows a plunging upper tip region geometry, i.e. the tip line plunges down from the central part of a fault plane towards the lateral tip regions (Childs et al., 1993; Nicol et al., 1996; Childs et al., 2003). The tip zone of growth faults is characterised by presenting relatively horizontal lines, only exhibiting offsetting adjacent strata in throw contours, from sub-vertical to sub-horizontal, when a significant proportion of the total displacement is accrued (Petersen et al., 1992; Baudon and Cartwright, 2008c). If different faults tip-out upwards at a

single horizon, these faults are likely growth faults, rather than blind faults (Baudon and Cartwright, 2008b).

In our case, the upper tip lines of the normal faults terminating after 5.5 Ma (Faults 1, 2 and 3) resemble sub-horizontal lines (e.g. Fig. 8a, b and c), indicating that faults cutting through T30 are growth faults. The upper tip lines of Faults 2 and 3 are observed at the same horizon (~450 ms below the sea floor; Figs. 8b and c), demonstrating that Faults 2 and 3 can be interpreted as growth faults. However, normal faults whose upper tips did not reach T30 (5.5 Ma) show significant differences in the location of their upper tip lines (Fig. 8d). This provides clear evidence that normal faults terminating in the strata older than 5.5 Ma are blind faults.

The other line of evidence involves the presence of upper tip propagation folds, which are frequently associated with the upward propagation of blind normal faults. The presence of upper tip propagation folds has been regarded as a key criterion for recognising blind faults (see Withjack and Callaway, 2000). The strata above the upper tips of normal faults that terminate above T30 (5.5 Ma) are characterized as parallel, continuous seismic reflections (Fig. 9b). However, propagation folds can be observed above the upper tips of normal faults that are truncated below T30 (Fig. 9e).

It was noted that there is no obvious stratigraphic thickening in the hanging wall of the faults which are truncated below T30 in our study area. The absence of evidence of faults interaction with the seabed supports the interpretation that these faults are blind; however, resolution and scale problems may sometimes give rise to the absence of these indicators (e.g. Cartwright et al., 1998; Baudon and Cartwright, 2008c). Hence, considering the combination of three criteria proposed by Baudon and Cartwright (2008c) and the evidence found in the study area, we theorise that normal faults growing after 5.5 Ma are growth faults, while those inactive before 5.5 Ma are blind faults.

5.2 Reactivation model of normal faults on the northwest South China Sea

According to the observations described above, two different styles of normal faulting, occur in the study area. Growth faults offsetting Horizon T30 (~5.5 Ma) comprise a gently-dipping (~18° to 31°) section in the Middle and Upper Miocene strata, and more steeply-dipping (>40°) upper portions at Pliocene and Quaternary levels (e.g. Figs. 4a and 9a). Significant changes in the dip of growth faults across T30 indicate that they were reactivated after 5.5 Ma. We notice that the dips of growth faults in their lower portion (Middle and Upper Miocene strata) are almost identical to those of blind faults. The dips of blind faults in Middle and Upper Miocene strata (older than ~5.5 Ma) range from 17° to 31° (Fig. 9d). Additionally, similar variation trends can be observed in the T-z plots (e.g. throw gradients and geometry) when comparing the lower portion of growth faults and blind faults (Figs. 8c and d). Therefore, we propose that the lower portions of the growth faults were buried and blind before 5.5 Ma, with some of the blind faults being reactivated after 5.5 Ma to form growth faults.

To complement our analysis, fault propagation on the continental shelf of the northwest South China Sea was reconstructed over a period spanning Miocene to the Quaternary. A three-stage evolutionary model is therefore proposed for the normal faults in our study area (Fig. 10), and the T-z plots of faults exemplify this three-stage fault growth model (Fig. 8).

Stage I: The first stage occurred before 5.5 Ma, numerous normal faults intersected the Miocene strata (Fig. 10a). Vertical throw plots for these faults show features akin to blind faults (Fig. 8d). The average T-z plot of these blind faults is characterised by broad central region and very gentle throw gradients (Figs. 8d and 10a).

Stage II: Some of the blind faults changed into small growth faults (Fig. 10b). T-z plots

show differences between both kinds of faults after this stage (Figs. 10b and 8). Difference in the dips of growth and blind faults are established at this stage (Fig. 4a, 9a, 10b and 11d).

Stage III: The final stage for the evolution of normal faults on the northwestern South China Sea margin lasted from Pliocene to the Quaternary. Most growth faults were still active during the Quaternary and some terminated close to the present sea floor (Fig. 4a, 9a, 10c and 11d).

5.3 Factors controlling the reactivation of blind faults in the South China Sea

5.3.1 Rotation of the South China block and slip reversal of the Ailao Shan-Red River Fault Zone at ~5.5 Ma

The rotation of South China could explain the mechanisms of faulting in the study area. The S-SE push of the Tibetan plate pushed the South China Sea Plate in an eastward motion inducing its forward clockwise rotation (Replumaz and Tapponnier, 2003; Van Hinsbergen et al., 2011). The movement of both plates made Indochina to spin clockwise on itself (Replumaz and Tapponnier, 2003). In addition, the rotation of both plates made the strike of the Red River Fault roughly rotate around the pole since then (Jolivet et al., 1999; Li et al., 2017). The Indochina rotated slower along its Red River boundary than the South China block after 5.5 Ma, resulting in dextral slip of the Ailao Shan-Red River Fault Zone (Replumaz et al., 2001). Deformation episodes in the offshore Ailao Shan-Red River Fault Zone include a period of sinistral movement (~30 to 16 Ma), a transitional phase (16 to 5.5 Ma), and a period of dextral movement after 5.5 Ma (Fig. 11 a-c; e.g. Replumaz et al., 2001; Sun et al., 2003; Zhu et al., 2009)

Under the influence of the rotation of the South China plate, changes in the styles of faulting in the study area are inferred to be related to slip reversal of the Ailao Shan-Red River Fault Zone at ~5.5 Ma. Although the trend of the offshore Ailao Shan-Red River Fault Zone did not go through our study area, the tectonic evolution of the Qiongdongnan Basin is closely linked to the significant strike-slip movements recorded in the Ailao Shan-Red River Fault Zone (Zhao et al., 2015). According to previous studies, the Late Miocene reversal in the movement of the Ailao Shan-Red River Fault Zone affected the Qiongdongnan Basin (Gong et all., 2011). Wang et al. (2016) have identified a large-scale Late Miocene submarine landslide, which was triggered by the reversal of the Ailao Shan-Red River Fault Zone in this basin. The existence of inverted faults and subsequent changes of sedimentary rates were also recorded during the Miocene (Clift and Sun, 2006; Zhu et al., 2009).

The average K values of T-z plots in our study area changed from negative to positive at ~5.5 Ma, meaning that the normal faults in the study area recorded a reversal in movement in the Late Miocene. Confirming this latter interpretation, most faults below T30 (~5.5 Ma) are blind faults, while faults terminating above T30 are growth faults. Throw maxima are recorded at ~5.5 Ma and most faults terminate below T30. These results suggest that the factors affecting the fault were weakening and reversing??? Not clear at ~5.5 Ma, which provides direct evidence for the slip reversal associated with the Red River Fault. The slip reversal in the Ailao Shan-Red River Fault Zone occurred at almost the same time, changing from a relatively quiet period (16-5.5 Ma) to a relatively slow dextral movement (5.5 Ma to present) (e.g. Zhu et al., 2009). Hence, there is a clear relationship amongst the time, relative movement of the Ailao Shan-Red River Fault Zone, and the reactivation of blind faults in the study area (~ 5.5 Ma) (Fig. 11).

5.3.2 Widespread slope instability at ~ 5.5 Ma

Post-rift subsidence on continental margins is mainly governed by thermal relaxation, sediment loading and contraction of the lithosphere (Wei et al., 2001; Wu et al., 2009;

Zhao et al., 2018a; Zhao et al., 2019). It gives rise to new faults and promotes the reactivation of pre-existing faults (Xie et al., 2006). In the study area, the post-rift tectonic phase started in the Miocene and total tectonic subsidence varied from 0 to 600 m during the Early and Middle Miocene, i.e. recording smaller values of subsidence than during the Late Miocene and Quaternary (Xie et al., 2006; He et al., 2013). Rapid tectonic subsidence occurred during the Late Miocene (11.6–5.5 Ma), possibly as the dynamic support induced by mantle convection was reduced (Zhao et al., 2018a), a phenomenon previously associated with continental breakup in Soares et al. (2012), Zhao et al. (2016) and Alves and Cunha (2018). Dong et al. (2020) also noticed the subsidence rate on the continental shelf of Qiongdongnan Basin was slow from the Early to Middle Miocene and abruptly increased from the Late Miocene. Post-rift subsidence slowed again from Pliocene to the Quaternary (5.5–0 Ma) (Zhao et al., 2018a). Both of these factors led to a peak in depositional rates in the Qiongdongnan Basin after 5.5 Ma (Clift and Sun, 2006; Zhao et al., 2015). Previous work has proved there is an abruptly increased subsidence rate during the Late Miocene in the study area (Clift and Sun, 2006; Zhao et al., 2015; Zhao et al., 2018a; Dong et al. 2020). As a result, mass-transport deposits are observed on the adjacent slope (He et al., 2013; Li et al., 2015), suggesting that slope instability became frequent on the northwest South China Sea margin after 5.5 Ma. Slope instability after 5.5 Ma could be one of the factors which have a vital impact on the propagation of faults in our study area.

This work infers that the evolution of normal faults in the Qiongdongnan Basin was controlled by variations in local stresses due to sediment loading at ~5.5 Ma. The relationship between fault activity and sedimentation rates was proved in Baiyun Sag (Sun et al., 2014). In our study area, there is also a correlation between the incision of submarine canyons at the shelf break and the presence of normal faults, especially those of greater length (He et al., 2013). The faults along the continental shelf were triggered by large-scale slope instability (Lei and Ren, 2016). These previous studies point to subsidence of sediments in the shelf influence the evolution of faults. T_{max} of faults could strongly support this viewpoint. In the study area, maximum fault throws tend to decrease from south to north ($T_{max\ Fault1} > T_{max\ Fault2} > T_{max\ Fault3}$) (Fig. 8). Slope instability can also explain why the normal faults to the south have larger throws than those to the north, and why the former also ceased after faults were formed to the north (Figs. 6 and 7). Based on the T_{max}, period of activity and termination time of the faults, we conclude the slope instability was one of the reasons that influence the evolution of faults on the continental shelf of Qiongdongnan Basin.

5.4 Implications

As one of the largest marginal seas in the Western Pacific Ocean (Fig. 1), the South China Sea provide an ideal laboratory platform for the research of geometric and kinematic analysis of normal faults (e.g. Huang et al. 2018; Lei et al., 2019). This study indicated there are two types of faults on the shelf of the northwest South China Sea and the faults reactive during 5.5 Ma. The rotation of the South China block and slip reversal of the Ailao Shan-Red River Fault Zone play an important role in the evolution of fault systems on the continental shelf of the northwest South China Sea has been proved in our study area. Our research improves understanding on the propagation and reactivation history of normal faults on the continental shelf of the northwest South China Sea, especially after the Late Miocene.

High-resolution 3D seismic data from the Qiongdongnan Basin provide an opportunity to clarify a new propagation model of faults on its continental shelf. Faults terminating before 5.5 Ma can be interpreted as blind faults, and some of them propagated further to become growth faults after 5.5 Ma, terminating in Quaternary

strata. Our model captures a specific period of the fault reactive because of block rotation and slip reversal of regional tectonic faults. Slope instability caused by abnormal sediment subsidence rates also is an important factor for the reactivity of faults on the edge of the shelf. We also noticed the strike of the fault system (WNW) is oblique to the edge of continental margins and the Hainan Island coastline which is approximate NE of the study area (Figs 1 and 6). Previous studies in the Australian shelf area or Brazilian shelf have suggested that the faults extend parallel to the coastline (Black et al., 2017; Deng and McClay, 2019). The strikes of the faults can be controlled by multiple factors such as regional tectonic stress, tectonic subsidence, and lithology (Ye et al., 2018). In our study area, the interpretation of control factors for the strike of fault should firstly take into account its regional tectonic stress and sediment accumulation after the Late Miocene.

6 Conclusions

High-resolution 3D seismic reflection data allowed us to reveal, for the first time, the distribution, orientations and evolution history of normal faults on the continental shelf of the northwest South China Sea. The main conclusions of this study are as follows:

(a) Sixty-six (66) normal faults are identified and they show a prominent WNW orientation. Small-scale (<5 km long) faults are concentrated in the northern part of the study area, while few large-scale faults (5-20 km long) are located towards the south.

(b) The vast majority of normal faults in the study area offset Middle Miocene to Pliocene strata, terminating at the Quaternary level. These faults show depth-dependent changes in dip, with the northern faults terminated earlier than those in the south.

(c) Faults terminating below T30 can be interpreted as blind faults, and some propagated further to become growth faults after 5.5 Ma, terminating in Quaternary strata. A three-stage model is therefore proposed to explain their evolution history.

(d) The propagation of normal faults on the continental shelf of the northwest South China Sea, after the Late Miocene, can be attributed to: (1) the rotation of the South China block and a reversal in movement of the Ailao Shan-Red River Fault Zone, changing from a relatively quiet period (16-5.5 Ma) to a relatively active phase recording dextral movement (5.5 Ma to present), and (2) slope instability occurring on the northwestern South China Sea margin at ~ 5.5 Ma.

The detailed investigation of the normal faults in this work is of great significance for a better understanding of the structural framework and evolution of northwest South China Sea margin since the Late Miocene. It also provides clear evidence for the movement of margin-scale structures (e.g. the Ailao Shan-Red River Fault Zone), which where capable of affecting areas far from the main loci of tectonic activity.

Acknowledgments

We acknowledge China National Offshore Oil Corporation for their permission to release the seismic data. This work was financially supported by the Key Special Project for Introduced Talents Team of Southern Marine Science and Engineering Guangdong Laboratory (Guangzhou) (GML2019ZD0104), National Key Research and Development Program of China (2017YFC1500401) and National Natural Science Foundation of China (41876054). Dr. Wei Li is funded by CAS Pioneer Hundred Talents Program (Y8SL011001). We are grateful to the editor and two anonymous reviewers for their thorough and constructive comments.

References

Alves, T.M., Cartwright, J., Davies, R.J., 2009. Faulting of salt-withdrawal basins during early halokinesis: Effects on the Paleogene Rio Doce Canyon system (Espírito Santo Basin, Brazil). AAPG Bulletin 93, 617-652.

Baudon, C., Cartwright, J., 2008a. The kinematics of reactivation of normal faults using high resolution throw mapping. Journal of Structural Geology 30, 1072-1084.

Baudon, C., Cartwright, J., 2008b. Early stage evolution of growth faults: 3D seismic insights from the Levant Basin, Eastern Mediterranean. Journal of Structural Geology 30, 888-898.

Baudon, C., Cartwright, J.A., 2008c. 3D seismic characterisation of an array of blind normal faults in the Levant Basin, Eastern Mediterranean. Journal of Structural Geology 30, 746-760.

Black, M., McCormack, K.D., Elders, C., Robertson, D., 2017. Extensional fault evolution within the Exmouth Sub-basin, North West Shelf, Australia. Marine and Petroleum Geology 85, 301-315.

Cai, J., 2009. Paleo-morphologic restoration of Paleogene in Qiongdongnan Basin and its control on sequence architecture and sedimentary characteristics. China University of Geosciences.

Cartwright, J., Bouroullec, R., James, D., Johnson, H., 1998. Polycyclic motion history of some Gulf Coast growth faults from high-resolution displacement analysis. Geology 26, 819-822.

Cartwright, J.A., Trudgill, B.D., Mansfield, C.S., 1995. Fault growth by segment linkage: an explanation for scatter in maximum displacement and trace length data from the Canyonlands Grabens of SE Utah. Journal of Structural Geology 17, 1319-1326.

Chen, P.P.H., Chen, Z.Y., Zhang, Q.M., 1993. Sequence stratigraphy and continental-margin development of the northwestern shelf of the South China Sea. AAPG Bulletin 77, 842-862.

Childs, C., Easton, S., Vendeville, B., Jackson, M., Lin, S., Walsh, J., Watterson, J., 1993. Kinematic analysis of faults in a physical model of growth faulting above a viscous salt analogue. Tectonophysics 228, 313-329.

Childs, C., Delogkos, E., Manzocchi, T., Walsh, J.J., 2020. A geological record of changing propagation directions of fault slip events during the growth of a normal fault system. Tectonophysics 774, 228-296.

Childs, C., Nicol, A., Walsh, J.J., Watterson, J., 2003. The growth and propagation of synsedimentary faults. Journal of Structural Geology 25, 633-648.

Clift, P.D., Sun, Z., 2006. The sedimentary and tectonic evolution of the Yinggehai-Song Hong basin and the southern Hainan margin, South China Sea: Implications for Tibetan uplift and monsoon intensification. Journal of Geophysical Research: Solid Earth 111, 01-28.

Dawers, N.H., Anders, M.H., Scholz, C.H., 1993. Growth of normal faults: Displacement-length scaling. Geology 21, 1107-1110.

Deng, H., McClay, K., 2019. Development of extensional fault and fold system: Insights from 3D seismic interpretation of the Enderby Terrace, NW Shelf of Australia. Marine and Petroleum Geology 104, 11-28.

Dong, M., Zhang, J., Brune, S., Wu, S., Fang, G., Yu, L., 2020. Quantifying Postrift Lower Crustal Flow in the Northern Margin of the South China Sea. Journal of Geophysical Research: Solid Earth 125.

Gamberi, F., Rovere, M., Marani, M., 2011. Mass-transport complex evolution in a tectonically active margin (Gioia Basin, Southeastern Tyrrhenian Sea). Marine Geology 279, 98-110.

Giba, M., Walsh, J.J., Nicol, A., 2012. Segmentation and growth of an obliquely reactivated normal fault. Journal of Structural Geology 39, 253-267.

Gilley, L.D., Harrison, T.M., Leloup, P., Ryerson, F., Lovera, O.M., Wang, J.H., 2003. Direct dating of left-lateral deformation along the Red River shear zone, China and Vietnam. Journal of Geophysical Research: Solid Earth. 108.

Gomes, M.P., Vital, H., Bezerra, F.H.R., Castro, D.L., Macedo, Wang, J.W., 2014. The interplay between structural inheritance and morphology in the Equatorial Continental Shelf of Brazil. Marine Geology 355, 150-161.

Gong, C., Wang, Y., Zhu, W., Li, W., Xu, Q., Zhang, J., 2011. The Central Submarine Canyon in the Qiongdongnan Basin, northwestern South China Sea: Architecture, sequence stratigraphy, and depositional processes. Marine and Petroleum Geology 28, 1690-1702.

Jolivet, L., Maluski, H., Beyssac, O., Goffé, B., Lepvrier, C., Thi, P.T., Vuong, N.V., 1999. Oligocene-Miocene Bu Khang extensional gneiss dome in Vietnam: Geodynamic implications. Geology 27.

Han, J., Leng, J., Wang, Y., 2016. Characteristics and genesis of the polygonal fault system in southern slope of the Qiongdongnan Basin, South China Sea. Marine and Petroleum Geology 70, 163-174.

He, Y., Xie, X., Kneller, B.C., Wang, Z., Li, X., 2013. Architecture and controlling factors of canyon fills on the shelf margin in the Qiongdongnan Basin, northern South China Sea. Marine and Petroleum Geology 41, 264-276.

Huang, K., Zhong, G., He, M., Liu, L., Wu, Z., Liu, X., 2018. Growth and linkage of a complex oblique-slip fault zone in the Pearl River Mouth Basin, northern South China Sea. Journal of Structural Geology 117, 27-43.

Lei, C., Alves, T.M., Ren, J., Pang, X., Yang, L., Liu, J., 2019. Depositional architecture and structural evolution of a region immediately inboard of the locus of continental breakup (Liwan Sub-basin, South China Sea). GSA Bulletin 131, 1059-1074.

Lei, C., Alves, T.M., Ren, J., Tong, C., 2020. Rift Structure and Sediment Infill of Hyperextended Continental Crust: Insights From 3D Seismic

and Well Data (Xisha Trough, South China Sea). Journal of Geophysical Research: Solid Earth, 125.

Lei, C., Ren, J., 2016. Hyper-extended rift systems in the Xisha Trough, northwestern South China Sea: Implications for extreme crustal thinning ahead of a propagating ocean. Marine and Petroleum Geology 77, 846-864.

Lei, C., Ren, J., Clift, P.D., Wang, Z., Li, X., Tong, C., 2011. The structure and formation of diapirs in the Yinggehai–Song Hong Basin, South China Sea. Marine and Petroleum Geology 28, 980-991.

Lei, C., Ren, J., Sternai, P., Fox, M., Willett, S., Xie, X., Clift, P.D., Liao, J., Wang, Z., 2015. Structure and sediment budget of Yinggehai–Song Hong basin, South China Sea: Implications for Cenozoic tectonics and river basin reorganization in Southeast Asia. Tectonophysics 655, 177-190.

Leloup, P.H., Arnaud, N., Lacassin, R., Kienast, J., Harrison, T., Trong, T.P., Replumaz, A., Tapponnier, P.J., 2001. New constraints on the structure, thermochronology, and timing of the Ailao Shan-Red River shear zone, SE Asia. Journal of Geophysical Research: Solid Earth 106, 6683-6732.

Li, Q., Wang, P., Zhao, Q., Shao, L., Zhong, G., Tian, J., Cheng, X., Jian, Z., Su, X., 2006. A 33 Ma lithostratigraphic record of tectonic and paleoceanographic evolution of the South China Sea. Marine Geology 230, 217-235.

Li, S., Advokaat, E.L., van Hinsbergen, D.J.J., Koymans, M., Deng, C., Zhu, R., 2017. Paleomagnetic constraints on the Mesozoic-Cenozoic paleolatitudinal and rotational history of Indochina and South China: Review and updated kinematic reconstruction. Earth-Science Reviews 171, 58-77.

Li, W., Alves, T.M., Wu, S., Völker, D., Zhao, F., Mi, L., Kopf, A., 2015. Recurrent slope failure and submarine channel incision as key factors controlling reservoir potential in the South China Sea (Qiongdongnan Basin, South Hainan Island). Marine and Petroleum Geology 64, 17-30.

Maier, K.L., Brothers, D.S., Paull, C.K., McGann, M., Caress, D.W., Conrad, J.E., 2017. Records of continental slope sediment flow morphodynamic responses to gradient and active faulting from integrated AUV and ROV data, offshore Palos Verdes, southern California Borderland. Marine Geology 393, 47-66.

Mansfield, C., Cartwright, J., 1996. High resolution fault displacement mapping from three-dimensional seismic data: evidence for dip linkage during fault growth. Journal of Structural Geology 18, 249-263.

Muraoka, H., Kamata, H., 1983. Displacement distribution along minor fault traces. Journal of Structural Geology, 5, 483-495.

Nicol, A., Watterson, J., Walsh, J., Childs, C., 1996. The shapes, major axis orientations and displacement patterns of fault surfaces. Journal of Structural Geology 18, 235-248.

Omosanya, K.O., Eruteya, O.E., Siregar, E.S.A., Zieba, K.J., Johansen, S.E., Alves, T.M., Waldmann, N.D., 2018. Three-dimensional (3-D) seismic imaging of conduits and radial faults associated with hydrothermal vent complexes (Vøring Basin, Offshore Norway). Marine Geology 399, 115-134.

Omosanya, K.O., Johansen, S.E., Harishidayat, D., 2015. Evolution and character of supra-salt faults in the Easternmost Hammerfest Basin, SW Barents Sea. Marine and Petroleum Geology 66, 1013–1028.

Perea, H., Gràcia, E., Martínez-Loriente, S., Bartolome, R., de la Peña, L.G., de Mol, B., Moreno, X., Iacono, C.L., Diez, S., Tello, O., Gómez-Ballesteros, M., Dañobeitia, J.J., 2018. Kinematic analysis of secondary faults within a distributed shear-zone reveals fault linkage and increased seismic hazard. Marine Geology 399, 23-33.

Petersen, K., Clausen, O., Korstgård, J., 1992. Evolution of a salt-related listric growth fault near the D-1 well, plate 5605, Danish North Sea: displacement history and salt kinematics. Journal of Structural Geology 14, 565-577.

Replumaz, A., Lacassin, R., Tapponnier, P., Leloup, P., 2001. Large river offsets and Plio-Quaternary dextral slip rate on the Red River fault (Yunnan, China). Journal of Geophysical Research: Solid Earth 106, 819-836.

Replumaz, A., Tapponnier, P., 2003. Reconstruction of the deformed collision zone Between India and Asia by backward motion of lithospheric blocks. Journal of Geophysical Research: Solid Earth 108.

Rovere, M., Gamberi, F., Mercorella, A., Leidi, E., 2014. Geomorphometry of a submarine mass-transport complex and relationships with active faults in a rapidly uplifting margin (Gioia Basin, NE Sicily margin). Marine Geology 356, 31-43.

Ru, K., Pigott, J.D., 1986. Episodic rifting and subsidence in the South China Sea. AAPG Bulletin 70, 1136-1155.

Searle, M.P., Yeh, M.-W., Lin, T.-H., Chung, S.-L.J.G., 2010. Structural constraints on the timing of left-lateral shear along the Red River shear zone in the Ailao Shan and Diancang Shan Ranges, Yunnan, SW China. Geosphere 6(4): 316-338..

Soares, D.M., Alves, T.M., Terrinha, P., 2012. The breakup sequence and associated lithospheric breakup surface: their significance in the context of rifted continental margins (West Iberia and Newfoundland margins, North Atlantic). Earth and Planetary Science Letters, 311-326.

Sun, Q., Wu, S., Lü, F., Yuan, S., 2010. Polygonal faults and their implications for hydrocarbon reservoirs in the southern Qiongdongnan Basin, South China Sea. Journal of Asian Earth Sciences 39, 470-479.

Sun, Z., Xu, Z., Sun, L., Pang, X., Yan, C., Li, Y., Zhao, Z., Wang, Z., Zhang, C., 2014. The mechanism of post-rift fault activities in Baiyun sag, Pearl River Mouth basin. Journal of Asian Earth Sciences 89, 76-87.

Sun, Z., Zhou, D., Zhong, Z., Zeng, Z., Wu, S., 2003. Experimental evidence for the dynamics of the formation of the Yinggehai basin, NW South China Sea. Tectonophysics 372, 41-58.

Tao, Z., Alves, T.M., 2016. The role of gravitational collapse in controlling the evolution of crestal fault systems (Espírito Santo Basin, SE Brazil). Journal of Structural Geology 92, 79-98.

Taylor, S.K., Nicol, A., Walsh, J.J., 2008. Displacement loss on growth faults due to sediment compaction. Journal of Structural Geology 30, 394-405.

Thorsen, C.E., 1963. Age of growth faulting in Southeast Louisiana. Gcags Transactions 13, 103-110.

Van, H. D, J. J., Kapp, P., Dupont, N., G., Lippert, P.C., DeCelles, P.G., Torsvik, T.H., 2011. Restoration of Cenozoic deformation in Asia and the size of Greater India. Tectonics 30.

Wadsworth Jr, A., 1953. Percentage of thinning chart--new technique in subsurface geology. AAPG Bulletin 37, 158-162.

Wang, D., Wu, S., Li, C., Yao, G., 2016. Submarine slide evidence for late Miocene strike-slip reversal of the Red River Fault. Science China Earth Sciences 59, 2231-2239.

Wang, D., Wu, S., Qin, Z., Spence, G., Lü, F., 2013. Seismic characteristics of the Huaguang mass transport deposits in the Qiongdongnan Basin, South China Sea: Implications for regional tectonic activity. Marine Geology 346, 165-182.

Walsh, J.J., Watterson, J., 1988. Analysis of the relationship between displacements and dimensions of faults. Journal of Structural Geology 10, 239-247.

Watterson, J., 1986. Fault dimensions, displacements and growth. Pure and Applied Geophysics 124, 365-373.

Wei, K., Cui, H., Ye, S., Li, D., Liu, T., Liang, J., Yang, G., Wu, L., Zhou, X., Hao, Y., 2001. High-precision sequence stratigraphy in Qiongdongnan Basin. Earth Science-Journal of China University of Geosciences 26, 59-66.

Willis, B., Reid, J.A., 1907. How should faults be named and classified?. Economic Geology 2, 295-308.

Withjack, M.O., Callaway, S., 2000. Active normal faulting beneath a salt layer: an experimental study of deformation patterns in the cover sequence. AAPG Bulletin 84, 627-651.

Wu, S., Yuan, S., Zhang, G., Ma, Y., Mi, L., Xu, N., 2009. Seismic characteristics of a reef carbonate reservoir and implications for hydrocarbon exploration in deepwater of the Qiongdongnan Basin, northern South China Sea. Marine and Petroleum Geology 26, 817-823.

Wu, Z., Hu, M., 2019. Neotectonics, active tectonics and earthquake geology: Terminology, applications and advances. Journal of Geodynamics 127, 1-15.

Xie, X., Müller, R.D., Li, S., Gong, Z., Steinberger, B., 2006. Origin of anomalous subsidence along the Northern South China Sea margin and its relationship to dynamic topography. Marine and Petroleum Geology 23, 745-765.

Xie, X., Müller, R.D., Ren, J., Jiang, T., Zhang, C., 2008a. Stratigraphic architecture and evolution of the continental slope system in offshore Hainan, northern South China Sea. Marine Geology 247, 129-144.

Xie, Y., Wang, Z., Tong, C., 2008b. Petroleum geology of Yacheng 13-1, the largest gas field in China's offshore region. Marine and Petroleum Geology 25, 433-444.

Ye, Q., Mei, L., Shi, H., Camanni, G., Shu, Y., Wu, J., Yu, L., Deng, P., Li, G., 2018. The Late Cretaceous tectonic evolution of the South China Sea area: An overview, and new perspectives from 3D seismic reflection data. Earth-Science Reviews 187, 186-204.

Zhang, C., Wang, Z., Sun, Z., Sun, Z., Liu, J., Wang, Z., 2013. Structural differences between the western and eastern Qiongdongnan Basin: evidence of Indochina plate extrusion and South China Sea seafloor spreading. Marine Geophysical Research 34, 309-323.

Zhao, F., Alves, T.M., Wu, S., Li, W., Huuse, M., Mi, L., Sun, Q., Ma, B., 2016. Prolonged post-rift magmatism on highly extended crust of divergent continental margins (Baiyun Sag, South China Sea). Earth and Planetary Science Letters 445, 79-91.

Zhao, R., Chen, S., Olariu, C., Steel, R., Zhang, J., Wang, H., 2019. A model for oblique accretion on the South China Sea margin; Red River (Song Hong) sediment transport into Qiongdongnan Basin since Upper Miocene. Marine Geology, 416.

Zhao, Y., Ren, J., Pang, X., Yang, L., Zheng, J., 2018a. Structural style, formation of low angle normal fault and its controls on the evolution of Baiyun Rift, northern margin of the South China Sea. Marine and Petroleum Geology 89, 687-700.

Zhao, Z., Sun, Z., Sun, L., Wang, Z., Sun, Z., 2018b. Cenozoic tectonic subsidence in the Qiongdongnan Basin, northern South China Sea. Basin Research 30, 269-288.

Zhao, Z., Sun, Z., Wang, Z., Sun, Z., Liu, J., Zhang, C., 2015. The high resolution sedimentary filling in Qiongdongnan Basin, Northern South China Sea. Marine Geology 361, 11-24.

Zhou, D., Ru, K., Chen, H.Z., 1995. Kinematics of Cenozoic extension on the South China Sea continental margin and its implications for the tectonic evolution of the region. Tectonophysics 251, 161-177.

Zhu, M., Graham, S., McHargue, T., 2009. The Red River Fault zone in the Yinggehai Basin, South China Sea. Tectonophysics 476, 397-417.

Zhu, W.L., Zhang, G.C., Yang, S.K., Li, X.X., 2007. Natural gas geology of sedimental basin on northern continental margin of South China Sea. Petroleum Industry Press, Beijing.

Figure Captions

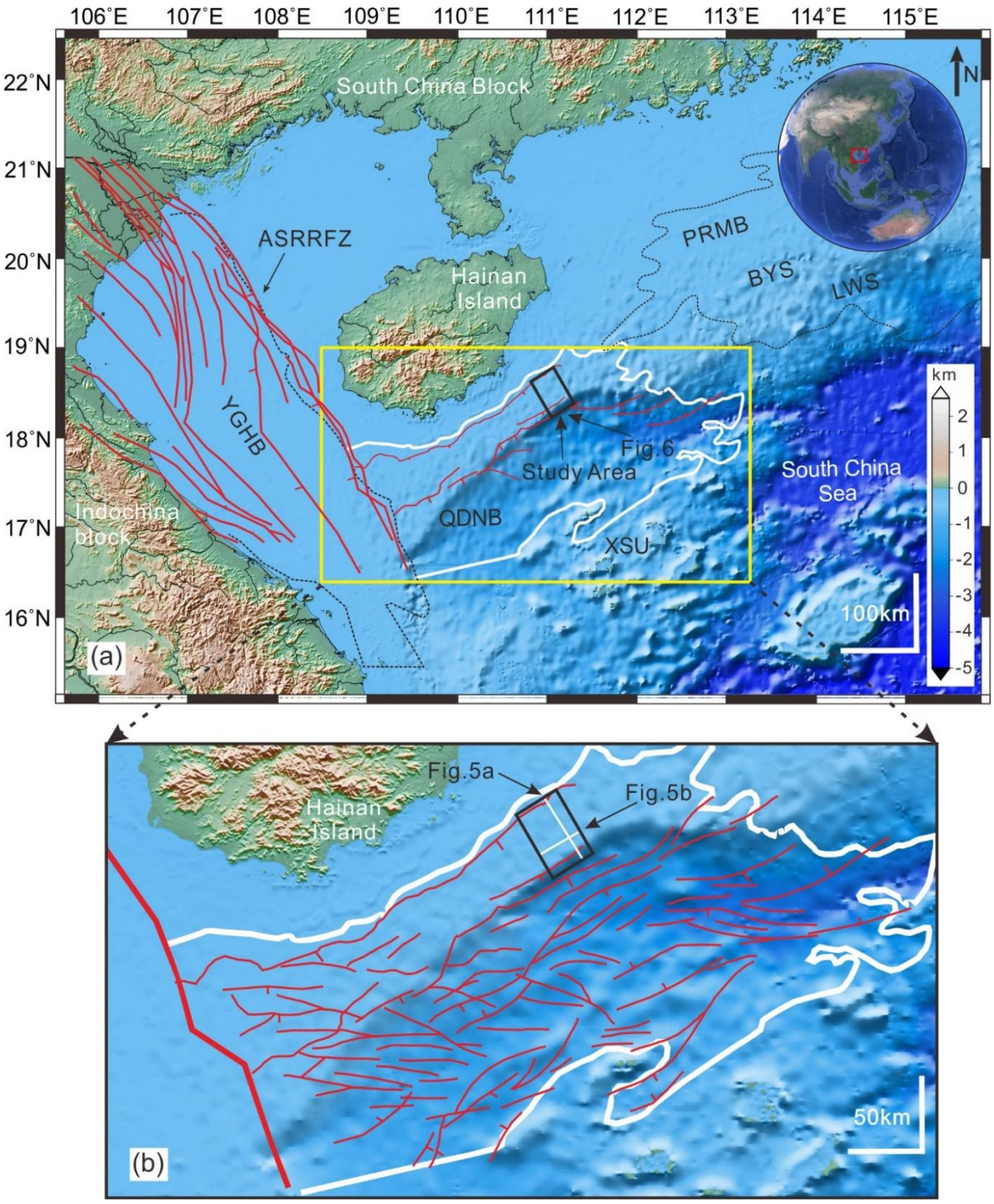

Fig.1 (a) Map of the northwest South China Sea showing the location of the study area and the Qiongdongnan Basin in relation to main faults. (b) A more detailed map of the Qiongdongnan Basin showing different fault systems. The black rectangle shows the location of the 3D seismic volume interpreted in this work. The white outline shows the location of the Qiongdongnan Basin in the South China Sea. The red solid lines indicate the distribution of faults on the northwest South China Sea margin (modified after Cai, 2009; Zhang et al., 2013; Lei et al., 2015; Lei and Ren, 2016). Abbreviations: QDNB= Qiongdongnan Basin; PRMB= Pearl River Mouth Basin; YGHB= Yinggehai Basin; ASRRFZ= Ailao Shan-Red River Fault Zone; XSU= Xisha Uplift; BYS= Baiyun Sag; LWS= Liwan Sag.

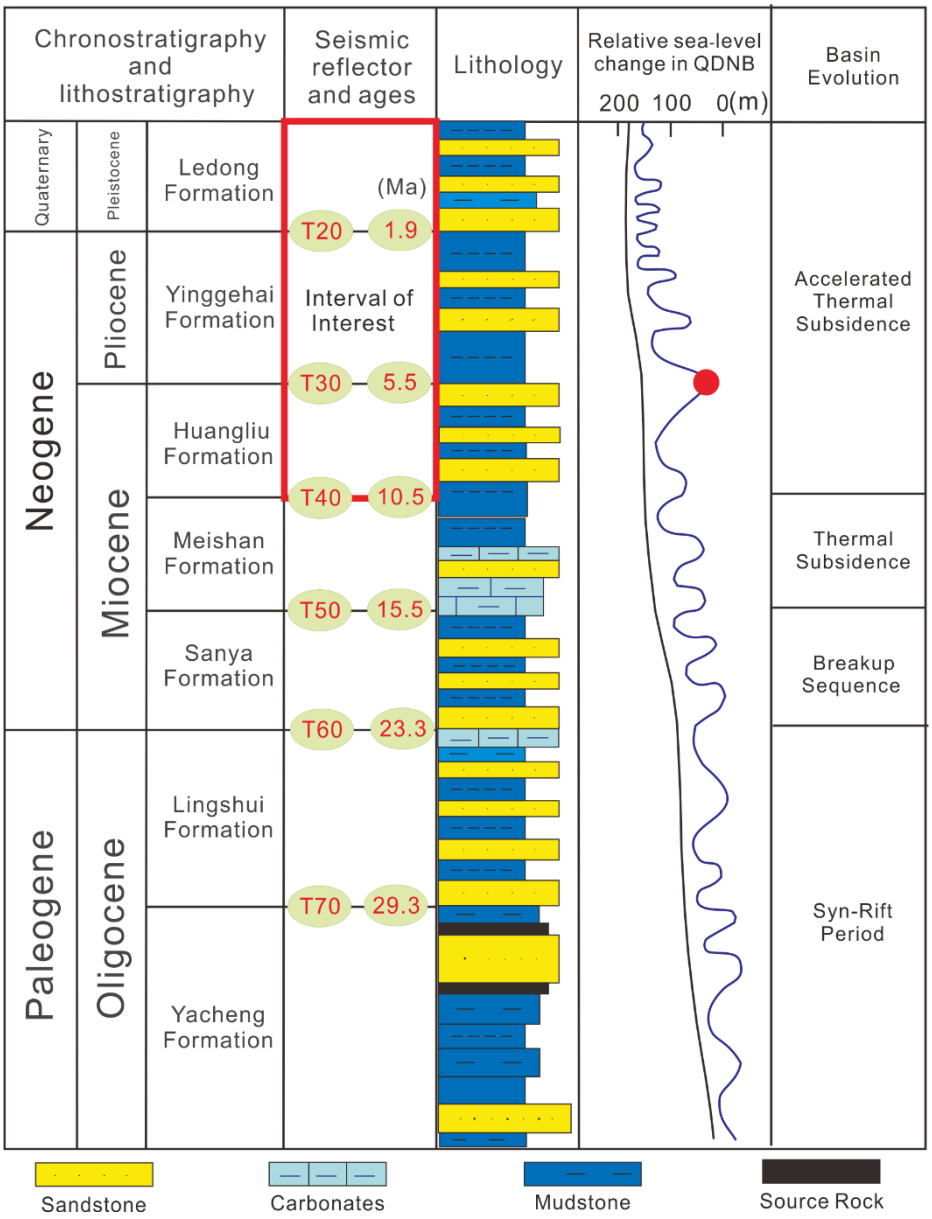

Fig. 2 Tectono-stratigraphic column of the Qiongdongnan Basin (Gong et al., 2011; Han et al., 2016; Xie et al., 2008b; Zhao et al., 2016). Relative sea-level changes in the Qiongdongnan Basin are based on Wei et al. (2001). The red rectangle indicated the interval of interest in our study. The red arrow points to the sea-level lowstand recorded at 5.5 Ma b.p.

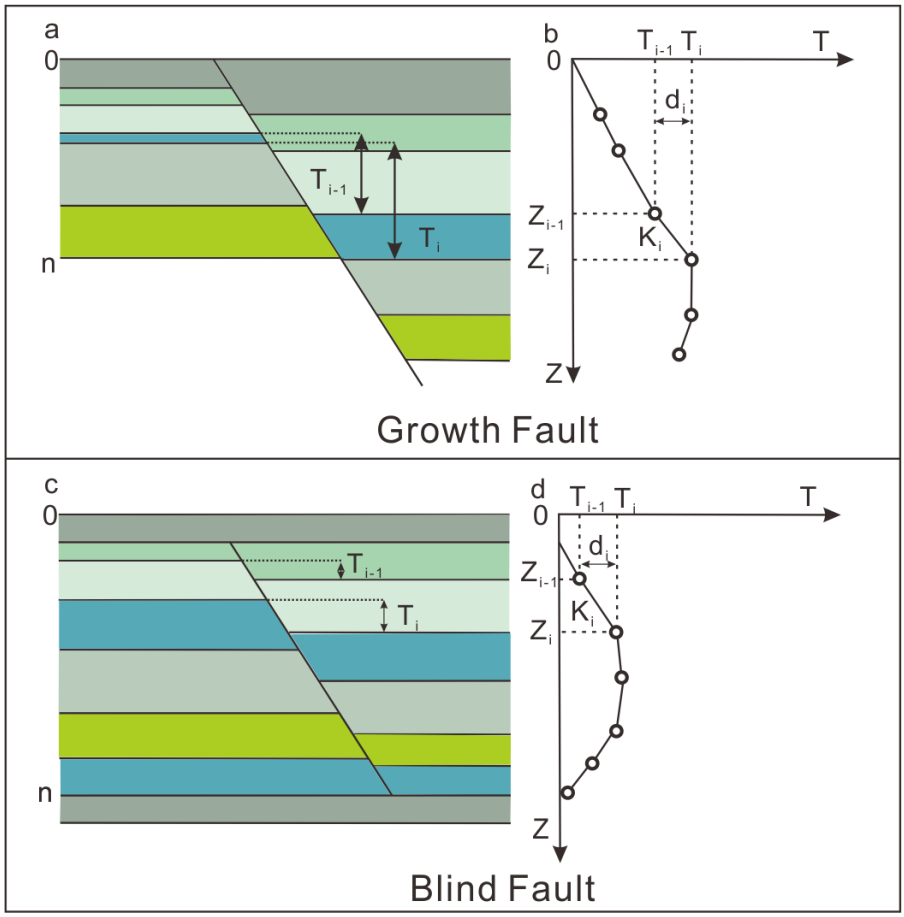

Fig. 3 (a) Cross-section of a growth fault (modified after Cartwright et al., 1998). (b) Corresponding T-z plot shows the relationships among vertical throw (T_i), displacement (d_i), stratigraphic thicknesses (T_i and T_{i-1}) and gradient (K_i) during one step of fault growth. The cross-section and T-z plot of a blind fault is shown in (c) and (d), respectively (modified after Baudon and Cartwright., 2008c).

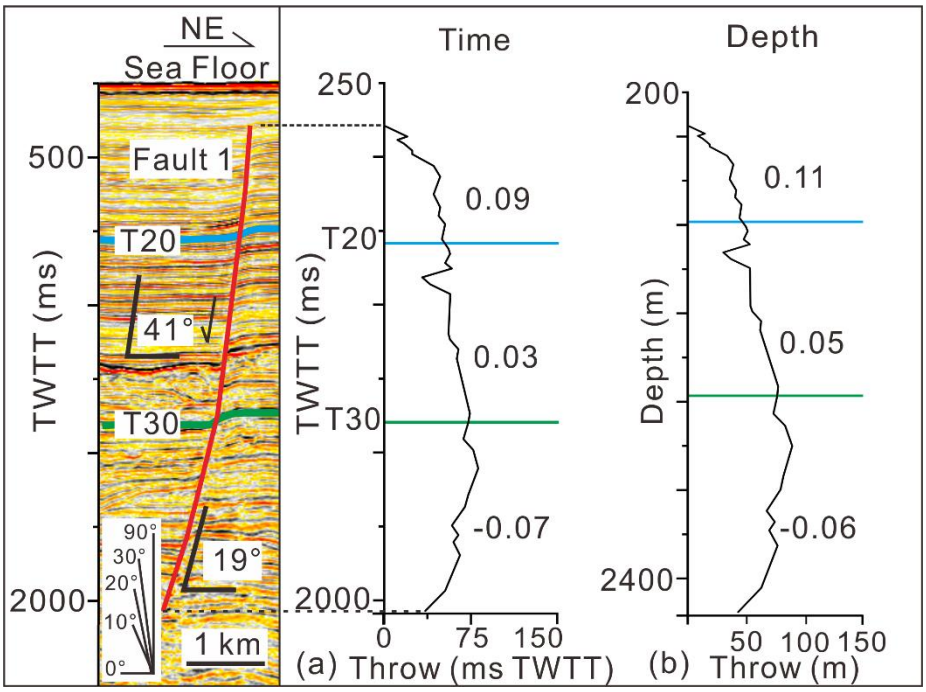

Fig. 4 Seismic profile crossing Fault 1 is shown on the left. The T-z plots of Fault 1 are shown in milliseconds (a) and meters (b), respectively. Depth converted T-z plots show a similar overall pattern in depth and time. Blue and green lines represent sequence boundaries T20 and T30, respectively. The dip of Fault 1 is also shown in the figure.

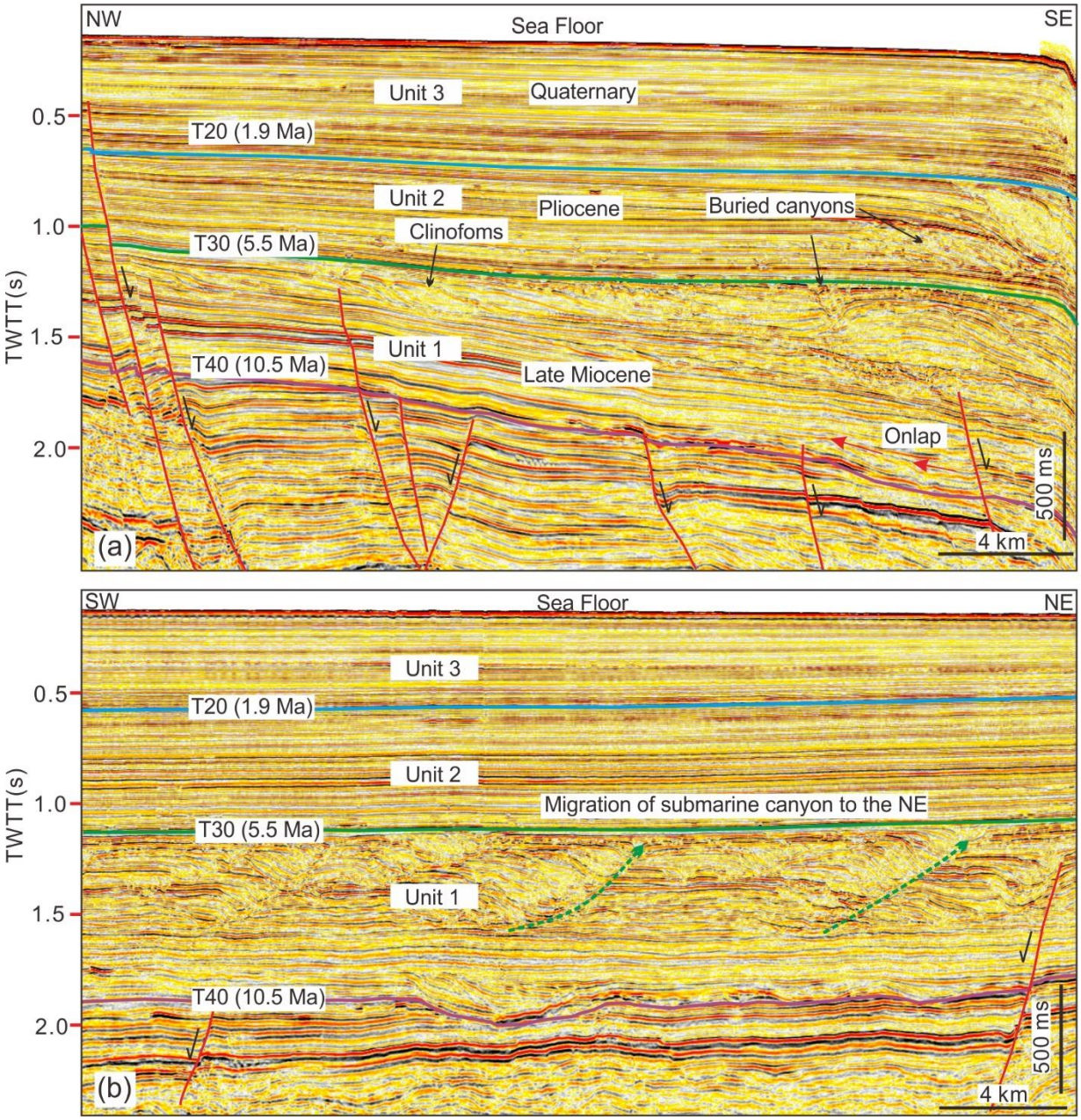

Fig. 5. (a) 2D seismic profile extracted from a 3D dataset crossing the middle part of research area to show numerous normal faults and buried submarine canyons. Note that three main stratigraphic units (Units 1, 2 and 3) were interpreted based on the differences in their internal seismic characters. (b) NE-trending seismic profile across the study area. Here, the buried submarine canyons in Unit 1 show a clear NE migration trend. Location of seismic profiles in Fig. 1b.

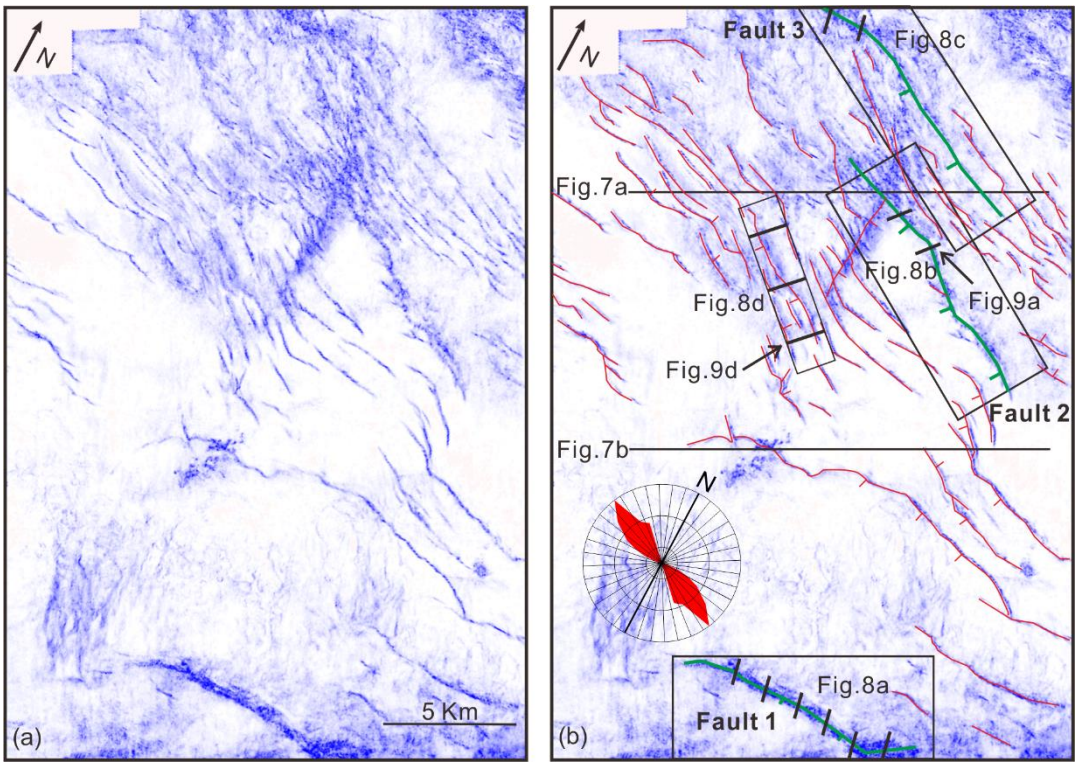

Fig. 6 (a) Uninterpreted variance time-slice at T=2 s in the study area. (b) Interpretation of the variance map highlighting the distribution of three major faults (Faults 1, 2 and 3 are marked in green) and numerous small-scale faults (red solid line). The rose plot stresses the predominant WNW orientation of the interpreted faults.

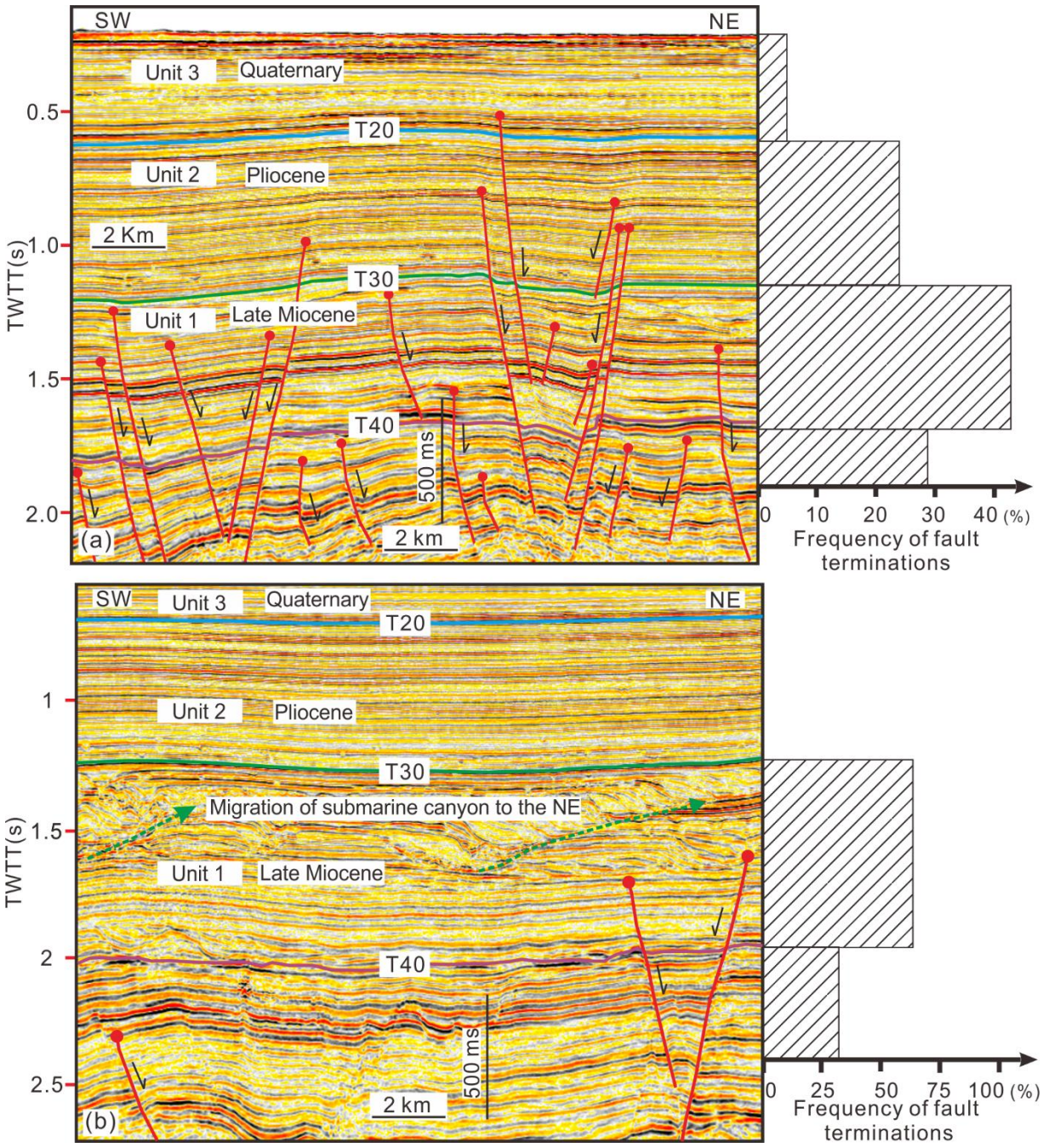

Fig. 7 (a) Seismic profile located in the northern part of the study area highlighting the frequency of fault terminations within different seismic units. Note that most of the faults terminate below Horizon T30 (5.5 Ma). (b) Seismic profile illustrates the frequency of fault terminations in the central part of the study area. Please see the location of seismic profiles in Fig. 6b. Red dots indicate the location of the terminations.

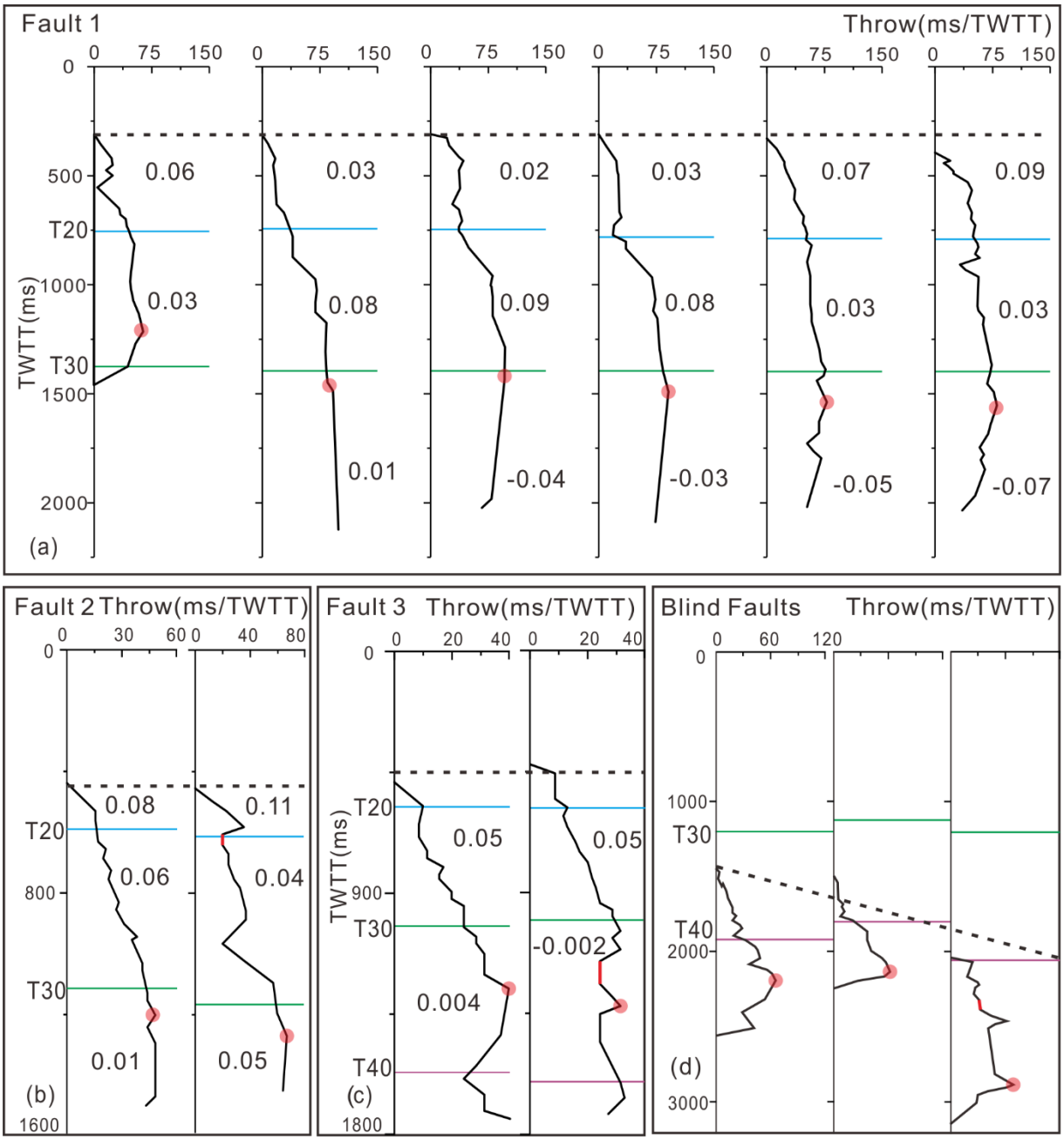

Fig. 8 (a) T-z plots of six seismic sections crossing Fault 1 from west to east. The dotted line represents the upper tip line of the T-z plots. (b) T-z plots of two seismic sections crossing Fault 2 from northwest to southeast. (c) T-z plots of two seismic sections crossing Fault 3 from northwest to southeast. (d) Faults that terminate beneath Horizon T30 are characterized by plunging down-tip lines. Blue, green and purple lines represent Horizons T20, T30 and T40, respectively. Yellow lines reveal the zero or near-zero gradient segments of the T-z plots. The red points indicate the maximum throw of the T-z plots. The gradient values on the T-z plots are annotated. Location of seismic sections used to compile the T-z plots in Fig. 6b.

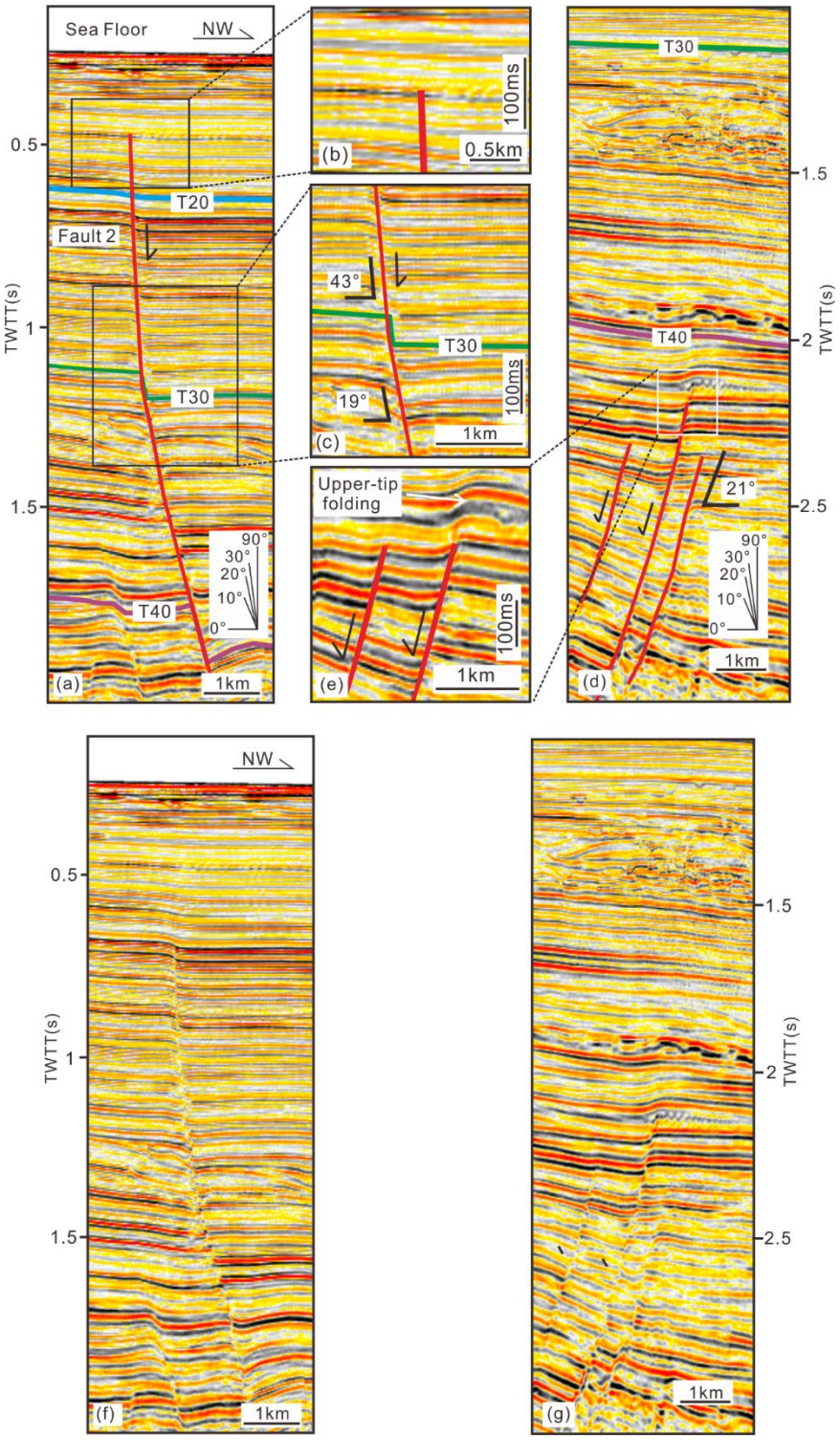

Fig. 9 (a) Seismic profile crossing the western tip of Fault 2 to reveal its geometry and upper tip terminations in Quaternary strata. (b) Zoomed seismic section showing the seismic characteristics of strata close to the upper tip of Fault 2. Note that the seismic reflections above the upper tip of Fault 2 are continuous. (c) The dip of Fault 2 above Horizon T30 (~43°) is much steeper than that below T30 (~19°). (d) Seismic line revealing the geometry and dips of normal faults that terminate below Horizon T30. (e) Note that upper-tip propagation folds can be observed above the faults that ceased below Horizon T30 (5.5 Ma). (f) and (g) uninterpreted seismic profiles of (a) and (d), respectively. Locations of seismic profiles in Fig. 6b.

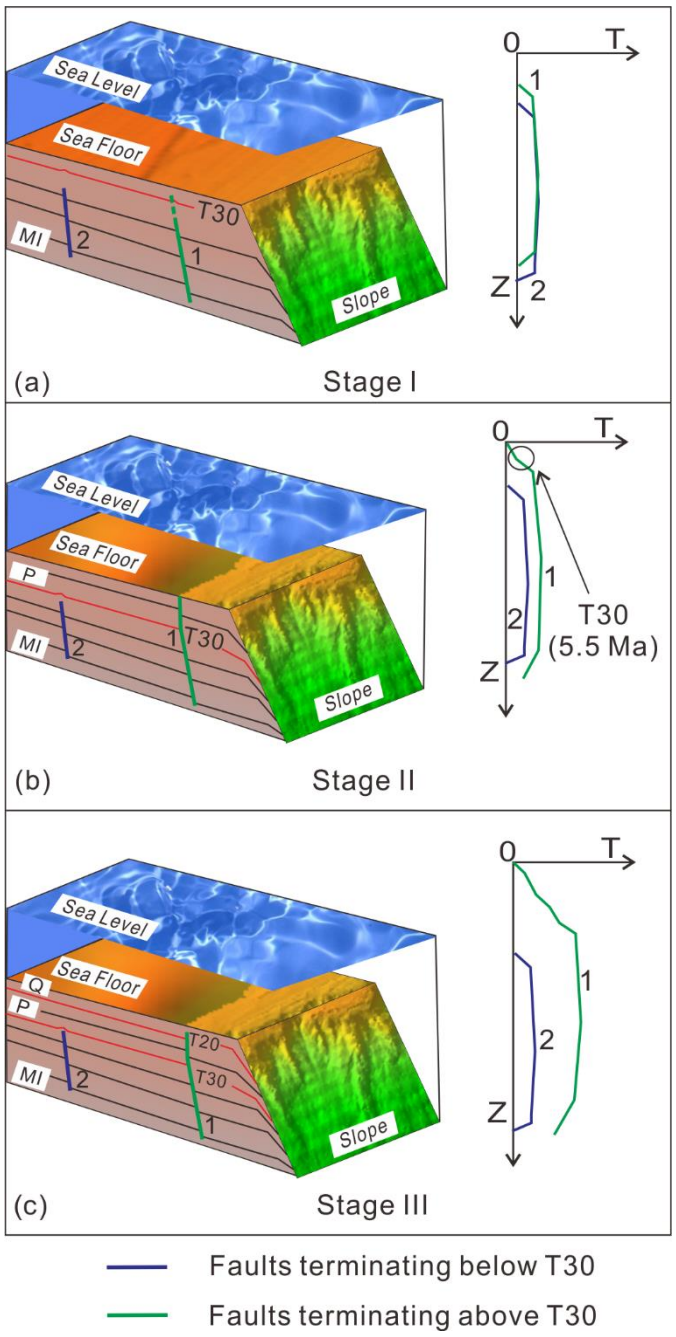

Fig. 10 Schematic model summarising the propagation styles of normal faults and associated variations in T-z plots in the study area. Stage I: Multiple blind faults are developed within Miocene strata. Stage II: Some of these blind faults change into growth faults (marked in green). Stage III: Growth faults are still active during the Quaternary and some terminate close to the sea floor.

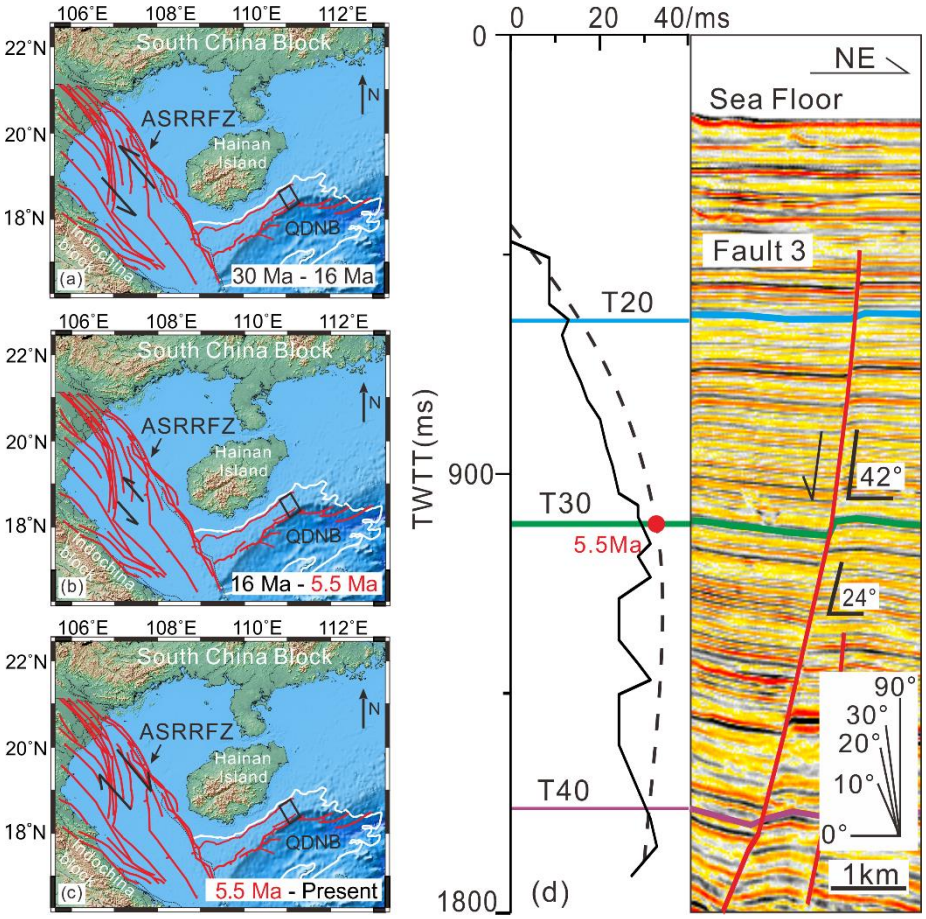

Fig. 11 Movement of the Ailao Shan-Red River Fault Zone included: (a) a predominant sinistral movement from ~ 30 to 16 Ma (b), a transitional phase between 16 and 5.5 Ma, and (c) a change to a predominant dextral movement after 5.5 Ma (Zhu et al., 2010). The black rectangle shows the location of the study area. (d) T-z plot of Fault 3 documenting the effect of slip reversal in the Ailao Shan-Red River Fault Zone at 5.5 Ma (T30). The dotted line represents the trend of the T-z plot according to the K value, and the red point indicates the reversal in the gradients of the T-z plot. The blue, green and purple lines represent horizons T20, T30 and T40 respectively. Abbreviations: QDNB= Qiongdongnan Basin; HI= Hainan Island; ASRRFZ= Ailao Shan-Red River Fault Zone.